Unleashing shear: Role of intercellular traction and cellular moments in collective cell migration

Neel G. Patel [a], Alyson Nguyen [b], Ningyong Xu [c, d], Shivani Ananthasekar [e], Diego F. Alvarez [f], Troy Stevens [c, d], Dhananjay T. Tambe [a, d, g, *]

[a] *William B. Burnsed, Jr. Department of Mechanical Engineering, College of Engineering, University of South Alabama, Mobile, AL, USA*
[b] *Department of Biomedical Sciences, Pat Capps Covey College of Allied Health Professions, University of South Alabama, Mobile, AL, USA*
[c] *Department of Physiology and Cell Biology, College of Medicine, University of South Alabama, Mobile, AL, USA*
[d] *Center for Lung Biology, College of Medicine, University of South Alabama, Mobile, AL, USA*
[e] *School of Medicine, University of Alabama at Birmingham, Birmingham, AL, USA*
[f] *Department of Physiology & Pharmacology, College of Osteopathic Medicine, Sam Houston State University, Conroe, TX, USA*
[g] *Department of Pharmacology, College of Medicine, University of South Alabama, Mobile, AL, USA*

ARTICLE INFO

ABSTRACT

In the field of endothelial biology, the term "shear forces" is tied to the forces exerted by the flowing blood on the quiescent cells. But endothelial cells themselves also exert physical forces on their immediate and distant neighbors. Specific factors of such intrinsic mechanical signals most relevant to immediate neighbors include normal (F_n) and shear (F_s) components of intercellular tractions, and those factors most relevant to distant neighbors include contractile or dilatational (M_c) and shear (M_s) components of the moments of cytoskeletal forces. However, for cells within a monolayer, F_n, F_s, M_c, and M_s remain inaccessible to experimental evaluation. Here, we present an approach that enables quantitative assessment of these properties. Remarkably, across a collectively migrating sheet of pulmonary microvascular endothelial cells, F_s was of the same order of magnitude as F_n. Moreover, compared to the normal components (F_n, M_c) of the mechanical signals, the shear components (F_s, M_s) were more distinctive in the cells closer to the migration front. Individual cells had an innately collective tendency to migrate along the axis of maximum contractile moment — a collective migratory process we referred to as *cellular* plithotaxis. Notably, larger F_s and M_s were associated with stronger plithotaxis, but dilatational moment appeared to disengage plithotactic guidance. Overall, cellular plithotaxis was more strongly associated with the "shear forces" (F_s, M_s) than with the "normal forces" (F_n, M_c). Finally, the mechanical state of the cells with fast migration speed and those with highly circular shape were reminiscent of fluid-like and solid-like matter, respectively. The results repeatedly pointed to neighbors imposing shear forces on a cell as a highly significant event, and hence, the term "shear forces" must include not just the forces from flowing fluid but also the forces from the substrate and neighbors. Collectively, these advances set the stage for deeper understanding of mechanical signaling in cellular monolayers.

1. Introduction

Endothelial cells possess the cytoskeletal apparatus that is capable of generating and transmitting contractile forces [1–3]. Across an endothelial monolayer, such forces propagate from each cell to its substrate and neighbors [4]. Such force propagation induces tractions across the cell-substrate and cell-cell interfaces. From a mechanical viewpoint, the distribution of tractions across the cell-substrate and cell-cell interfaces will have a strong influence on immediate neighbors, whereas resultant magnitude and moment of the tractions will have a strong influence on distant neighbors. A comprehensive assessment of tractions involves measurement of their magnitude and the direction of their action. Currently, however, such comprehensive assessment is only possible for the substrate tractions and not for the intercellular tractions and the moments of these tractions [5]. The inability to quantify such basic mechanical properties has significantly

* Corresponding author. William B. Burnsed, Jr. Department of Mechanical Engineering, College of Engineering, University of South Alabama, Mobile, AL, USA.
E-mail address: dtambe@southalabama.edu (D.T. Tambe).

narrowed the scope of the studies focused on mechanical signaling processes in cellular monolayers.

The substrate and intercellular tractions induce mechanical stresses across the monolayer. Monolayer Stress Microscopy (MSM) enabled a comprehensive assessment of thickness averaged monolayer stresses across such a monolayer [6,7]. At any subcellular region within the monolayer, MSM can identify maximum principal orientation along which normal stress (tensile or compressive stress) is highest and shear stress is zero [7]. Such orientation is central to the mechanical regulation of cellular motion, reorientation, and intercellular gap formation [6,8,9]. For example, in an advancing cellular monolayer, local cellular motion tends to be aligned with the local maximum principal orientation [6]. However, this phenomenon, described as plithotaxis, was identified by comparing motion and stresses defined over subcellular regions. The validity of plithotaxis has not been tested for maximum principal orientation and motion defined over an entire cell. Moreover, the physical significance of intercellular tractions in plithotactic guidance remains unexplored.

To address these knowledge gaps, we focused on an advancing sheet of pulmonary microvascular endothelial cells. We then described the approach that enables quantitative assessment of intercellular tractions and cellular moments [10]. To identify the physical significance of the intercellular tractions and cellular moments, we examined their distribution across the cellular monolayer and their relationship with cellular shape, speed, and plithotaxis. Surprisingly, compared to the normal components of intercellular forces and cellular moments, their shear counterparts were more strongly related to cellular shape, speed, and plithotaxis. Collectively, these findings open promising avenues for future research focused on the significance of fluid-like and solid-like behavior in the mechanics of cell monolayer.

2. Materials and methods

2.1. Cell culture and image acquisition

The cell culture procedure is the same as described in an earlier publication [11]. Briefly, rat pulmonary microvascular endothelial cells (rat 1, passage 11) were acquired from the cell culture core of the Center for Lung Biology at the University of South Alabama and cultured in 10% fetal bovine serum in a standard tissue culture environment. The data was acquired from cellular passages 12 through 16. Images were acquired using an inverted wide-field fluorescence microscope (Leica, DMI 600B) and confocal microscope (Nikon A1R). The data sets include three long (more than 940 min) and five short (more than 30 min) time-lapse sequences, each acquired at a 5 min interval.

2.2. Polyacrylamide hydrogel

The hydrogel preparation procedure was also the same as described in an earlier publication [11]. Briefly, all experiments were conducted in 35 mm glass-bottom dishes containing collagen-coated polyacrylamide hydrogels (1250 Pa shear modulus, approximately 100 μm thickness, 0.5 μm diameter embedded fluorescent beads).

2.3. Assessment of subcellular forces and motion

The subcellular forces and motion were also assessed as described in an earlier publication [11]. Briefly, components of substrate traction (T_i) were quantified using Fourier Transform Traction Microscopy (FTTM), monolayer stresses (σ_{ij}) were quantified using Monolayer Stress Microscopy (MSM) and the cellular motion was quantified using Particle Image Velocimetry (PIV) [5–7]. Since the substrate tractions and monolayer stresses are two-dimensional, the suffix i and j can be either x or y. The cross-correlation window size and spacing between adjacent windows were respectively 15.8 μm and 7.9 μm for PIV data analysis, and respectively 7.9 μm and 2.6 μm for both FTTM and MSM data analysis.

2.4. Assessment of intercellular tractions and cellular moments

The location of intercellular boundaries was detected from a phase-contrast image of the cellular monolayer using a custom image segmentation software (Fig. 1a) [11]. Through the pixels that defined intercellular boundary, we fitted a Fourier series with eight harmonics. This curve fitting enabled straightforward computation of unit normal (n_i) and tangent (t_i) vectors along the intercellular boundary (Fig. 1a). Normal (F_n) and shear (F_s) components of intercellular traction were computed using equations, $F_n = \sigma_{ij}n_jn_i$ and $F_s = \sigma_{ij}n_jt_i$ (Fig. 1b). Although these traction components were defined on a plane that is perpendicular to the monolayer, this approach can be applied to any angle between the plane that separates adjoining cells.

Components of the cellular moment were computed using $M_{ij} = \frac{1}{2}\left(-\int_A (T_ir_j + T_jr_i)d\mathbf{A} + \int_B (F_ir_j + F_jr_i)d\mathbf{B} \right)$, where r_i was the x or y coordinate where tractions were quantified and $\mathbf{A}$ is the area and $\mathbf{B}$ is the boundary of the cell as observed in the phase-contrast image. This definition of moment provides a positive number when moments are contractile representing tension in the cell, and a negative number when moments are dilatational representing compression of the cell. To compute principal moments M^{max} and M^{min}, we diagonalized the moment tensor using $\begin{bmatrix} M_{xx} & M_{xy} \\ M_{yx} & M_{yy} \end{bmatrix} = \begin{bmatrix} p_x & q_x \\ p_y & q_y \end{bmatrix} \begin{bmatrix} M^{max} & 0 \\ 0 & M^{min} \end{bmatrix} \begin{bmatrix} p_x & p_y \\ q_x & q_y \end{bmatrix}$, where p_i and q_i are the eigenvectors.

The orientation of maximum principal moment, M^{max}, was computed using $\theta_M = \arctan\left(p_y/p_x\right)$. The contractile or dilatational component of the cellular moment was computed using $M_c = \left(M^{max} + M^{min}\right)/2$. Maximum shear or anisotropy of the cellular moment was computed using $M_s = \left(M^{max} - M^{min}\right)/2$. It is important to note that for the lowest quintile of M_c, the median value was dilatational; but for the top four quintiles, the median values were contractile.

2.5. Physical properties considered in the data analysis

The circularity of the cell was computed using the formula, Circularity $= 4\pi$Area/Perimeter^2. To examine the significance of intercellular traction, we defined a ratio between its two components, $R = |F_s|/F_n$. This ratio assesses how other physical properties of individual cells are associated with (1) the relative magnitude of F_n and F_s, and (2) the orientation of intercellular traction. For each of the examined physical properties, we generated cumulative probability distribution from 300 randomly chosen frames each containing close to 300 cells.

Table 1
List of commonly used cellular properties and mathematical operators.

Property	Description (units)
P	Cumulative probability distribution (%)
v_i	Components of the average velocity of a cell (μm/min)
T_i	Components of the tractions exerted by the cell on the substrate (Pa)
σ_{ij}	Components of monolayer stresses (Pa)
F_s	Intercellular traction component oriented parallel to the intercellular interface (Pa)
F_n	Intercellular traction component oriented perpendicular to the intercellular interface (Pa)
R	Ratio of intercellular traction components, $\lvert F_s \rvert / F_n$
M_s	Shear moment or moment anisotropy of the cell (pN-m)
M_c	Contractile or dilatational moment of the cell (pN-m)
M^{max}	Maximum principal moment of the cell (pN-m)
θ_{Mv}	Angle between the orientation of M^{max} of the cell and the axis of net cellular velocity (°)
θ_{Cv}	Angle between the orientation of the cell and the axis of net cellular velocity (°)
θ_{CM}	Angle between the orientation of the cell and the orientation of M^{max} of the cell (°)
$(\dots)^{RMS}$	Root mean square value across the cell
$\lvert \dots \rvert$	Absolute value of the local property
$(\dots)^{SD}$	Standard deviation across the cell
$(\tilde{\dots})$	Median value across the cell
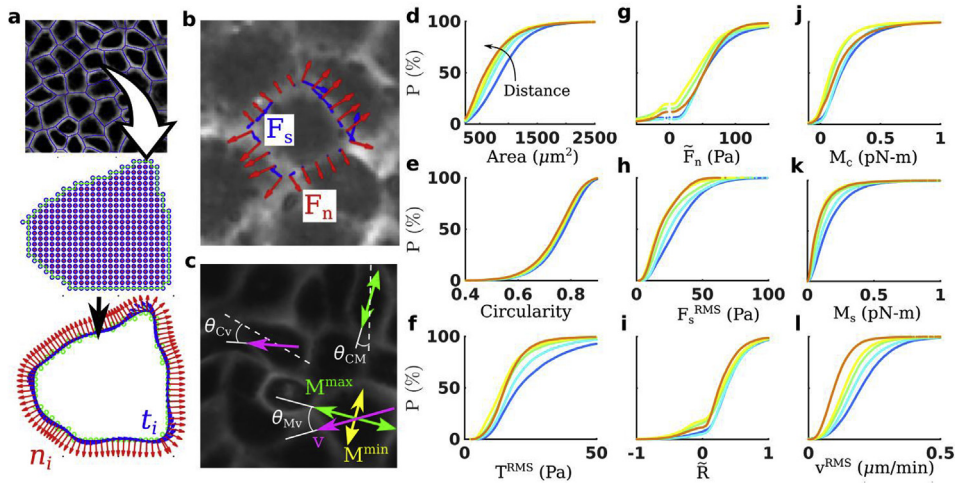
Fig. 1. Approach to quantify intercellular tractions and cellular moments, and distribution of these properties across the monolayer. a. Image of the cellular monolayer with intercellular boundaries (blue lines) identified using a custom segmentation software. The middle sub-panel shows pattern of sampling points where MSM provides T_i, and σ_{ij}. The bottom sub-panel shows unit vectors along normal (red arrows) and tangential (blue arrows) orientation. **b.** F_n (red arrows), and F_s (blue arrows), for a cell within the monolayer. **c.** Image of the cellular monolayer that illustrates including M^{max} (green arrow), M^{min} (yellow arrow), v (magenta arrow), cellular orientation (white dashed line), and angles θ_{Mv}, θ_{Cv}, and θ_{CM} (Table 1). The cumulative probability distribution of **d.** cellular spread area, **e.** cellular circularity, **f.** T^{RMS}, **g.** $\tilde{F}_n$, **h.** F_s^{RMS}, **i.** $\tilde{R}$, **j.** M_c, **k.** M_s, **l.** v^{RMS}. All cumulative distributions are plotted for quintiles of the distance of the centroid of the cell from the migration front. The lowest quintile is shown in blue and progressively higher quintiles are shown in progressively warmer colors. Arrow in panel **d** indicates progression from a lower quintile to a higher quintile. (For interpretation of the references to color in this figure legend, the reader is referred to the Web version of this article.)

3. Results

3.1. Distribution of tractions, moments, and other properties across the cellular monolayer

Compared to cells far from the migration front, cells near the migration front had several distinctive properties. Their morphological distinction included larger spread area and slightly larger circularity (Fig. 1d,e). Their distinctive mechanical state included larger T^{RMS}, F_s^{RMS}, M_s, and v^{RMS} (Fig. 1f,h,k,l and Table 1). However, these cells did not have a distinctive $\tilde{F}_n$, $\tilde{R}$, R^{SD}, or M_c (Figs. 1g,i,j and S1, and Table 1). Finally, the influence of cellular position with respect to the migration front was least striking for cellular circularity but most striking for v^{RMS} (Fig. 1d,e).

### 3.2. Relationships of intercellular tractions and cellular moments with cellular shape and speed

$\tilde{F}_n$ and F_s^{RMS} were weakly related to cellular circularity and speed (Fig. 2a—d). Both $\tilde{F}_n$ and F_s^{RMS} were larger in the cells that had lower circularity and faster speed. $\tilde{F}_n$ and F_s^{RMS} were independent of cellular spread area, but M_c and M_s were larger for the cells with bigger spread area (Fig. S2).

Cellular circularity and speed were not as strongly related to M_c as they were with the density of moment defined as M_c/Area (Figs. 2e,f and S3a,b, and Table 1). Similar enhancement of relationship was observed in M_s/Area versus cellular circularity but was not observed in M_s/Area versus cellular speed (Figs. 2g,h and S3c,d). M_c/Area and M_s/Area were larger in the cells with lower
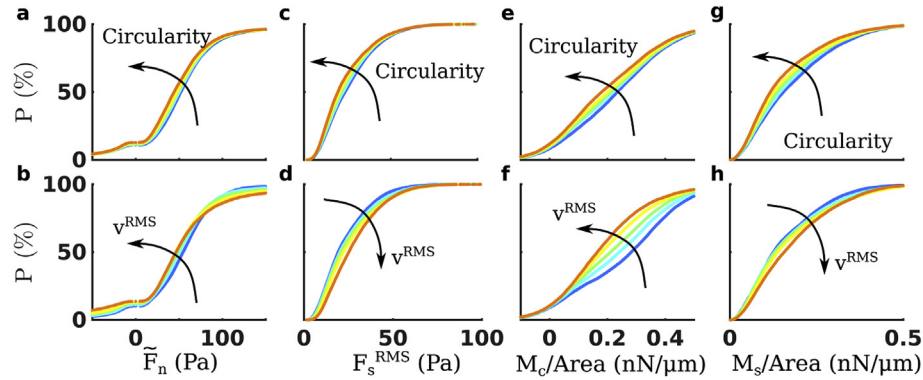
Fig. 2. Relationship of intercellular tractions and cellular moments with cellular shape and speed. The cumulative distribution of **a, b.** $\tilde{F}_n$, and **c, d.** F_s^{RMS}, **e, f.** M_c/Area, and **g, h.** M_s/Area. Cumulative distributions in the top row of panels are for quintiles of cellular circularity and those in the bottom row of panels are for quintiles of v^{RMS}. The lowest quintile is shown in blue and progressively higher quintiles are shown in progressively warmer colors. (For interpretation of the references to color in this figure legend, the reader is referred to the Web version of this article.)
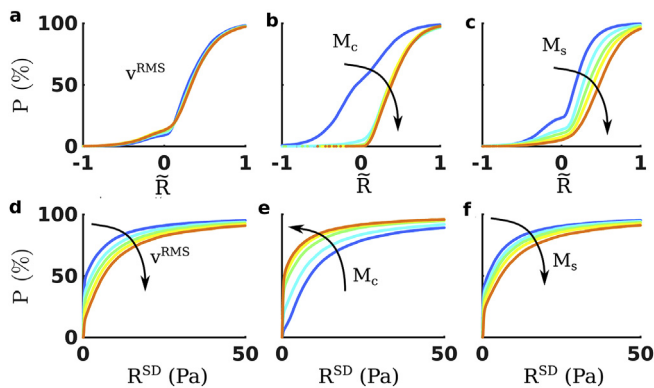
Fig. 3. Significance of median value and variability in intercellular traction orientation. The cumulative probability distribution of $\tilde{R}$, for quintiles of **a.** v^{RMS}, **b.** M_c, and **c.** M_s. The cumulative probability distribution of R^{SD} for quintiles of **d.** v^{RMS}, **e.** M_c and **f.** M_s. The lowest quintile is shown in blue and progressively higher quintiles are shown in progressively warmer colors. (For interpretation of the references to color in this figure legend, the reader is referred to the Web version of this article.)

circularity (Fig. 2e,g). Relationship between M_c/Area and v^{RMS} was opposite to that between M_s/Area and v^{RMS} (Fig. 2f,h). In that, faster cells had smaller M_c/Area but larger M_s/Area.
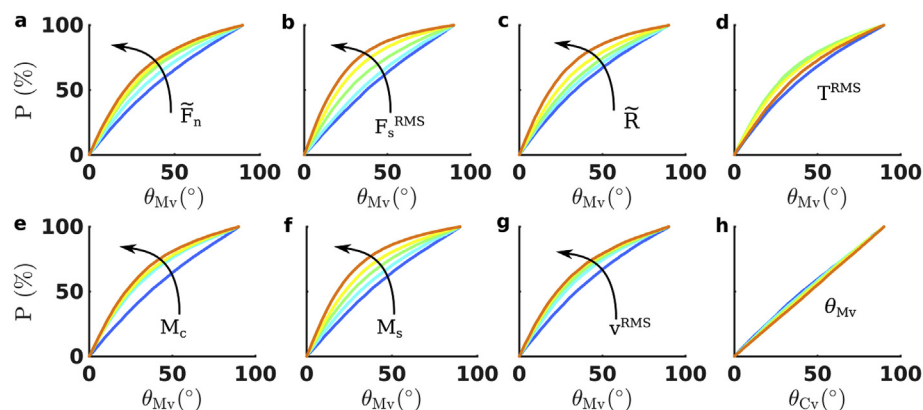
3.3. Relationships of intercellular traction orientation with cellular speed and moments

The distribution of $\tilde{R}$ was almost independent of v^{RMS} and top four quintiles of M_c, but $\tilde{R}$ systematically larger for higher quintiles of M_s (Fig. 3a–c). The lowest quintile of M_c which had a dilatational median value and large contributions from compressive F_n showed a distinct relationship (Fig. 3b, blue curve). Unlike the relationship with $\tilde{R}$, v^{RMS} and M_c had a stronger relationship with R^{SD} (Fig. 3d,e). By contrast, M_s was more strongly related with $\tilde{R}$ than with R^{SD} (Fig. 3c,f). Interestingly, M_c and M_s had an opposite relationship with R^{SD} (Fig. 3e,f).

3.4. Role of tractions, cellular moments, cellular speed, and cellular orientation in cellular plithotaxis

Smaller θ_{Mv} was associated with larger $\tilde{F}_n$, F_s^{RMS}, $\tilde{R}$, M_c, and M_s (Fig. 4a–c,e,f, and Table 1). The relationship was strongest for F_s^{RMS} (Fig. 4b). In contrast, the relationship was absent in the cells with compressive $\tilde{F}_n$ or dilatational M_c (Fig. 4a,e, blue curve).

Unlike the intercellular tractions, the substrate tractions did not have a systematic relationship with plithotaxis (Fig. 4a–d). Faster cells were associated with stronger plithotaxis, but stronger plithotaxis was not associated with smaller θ_{Cv} (Fig. 4g,h). However,

Fig. 4. Role of intercellular tractions, cellular moments, orientation, speed and traction in cellular plithotaxis. The cumulative probability distribution of θ_{Mv} for quintiles of **a.** $\tilde{F}_n$, **b.** F_s^{RMS}, **c.** $\tilde{R}$, **d.** T^{RMS}, **e.** M_c, **f.** M_s, and **g.** v^{RMS}. The cumulative probability distribution of θ_{Cv} for quintiles of **h.** θ_{Mv}. The lowest quintile is shown in blue and progressively higher quintiles are shown in progressively warmer colors. (For interpretation of the references to color in this figure legend, the reader is referred to the Web version of this article.)

cellular alignment with the axis of the principal moment and the axis of cellular motion appeared to be strongly proportional (Fig. S4).

4. Discussion

4.1. Visualizing fundamental intrinsic mechanical signals within individual cells of a monolayers

Both intrinsic and extrinsic mechanical signals induce structural and biochemical changes in individual cells of an adherent endothelial monolayer [12]. Early quantitative assessments of intrinsic mechanical signals involved measurement of isometric tension across the cellular monolayer [13]. Application of FTTM to cellular monolayer enabled quantitative assessment of the local adhesive forces transmitted to the extracellular matrix [5]. MSM enabled quantitative assessment of local mechanical stresses across the monolayer [6]. Scalar changes in tension across specific adhesion molecules, and net moments within an isolated individual cell, a doublet, and a small island have been measured [14–19]. However, for individual cells within a monolayer, two fundamental intrinsic signals remained hidden. First, individual components of the adhesive forces across the intercellular junction (F_n and F_s), and second, individual components of the moments across the cell (M_c and M_s). The approach described here quantifies these fundamental mechanical signals and enables the application of the principles of elasticity to better understand the mechanical interactions between immediate and distant neighbors.

4.2. The intercellular shear traction is a dominant mechanical signal

Substrate tractions were higher near the migration front than those far from it (Fig. 1f). Such traction distribution is observed in a variety of cell types [6]. A widely appreciated interpretation comes from a comparison of these tractions with force-balance in a tug-of-war [5]. But such comparison is made by adding tractions along a particular coordinate axis. The interpretation suggests that the monolayer is in a state of a "global" tug-of-war where the tension increases continuously from the advancing front to the center of the monolayer [5]. Importantly, in this interpretation, monolayer shear stresses along the same coordinate axis are assumed to be negligible.

While such interpretation is useful to appreciate the existence of intercellular force transmission, the inference that monolayer tension increases with the distance from the migration front can be misleading. In contrast with such inference, a rigorous force balance across the cellular monolayer revealed rather occasional regions — each spanning tens of cells — engaged in a "local" tug-of-war [6]. A striking contrast with the "global" tug-of-war model can be observed by comparing distributions of T^{RMS}, $\tilde{F}_n$, and M_c as a function of distance from the migration front (Fig. 1f,g,j). While T^{RMS} was systematically larger closer to the migration front, both $\tilde{F}_n$ and M_c had no systematic gradients. Moreover, compared to F_n, F_s was often smaller but far from negligible (Fig. 1i). Remarkably, F_s^{RMS} was larger for the cells located closer to the migration front (Fig. 1h). Such distribution revels the key source of the misleading inference form the "global" tug-of-war model — large portion of the interpreted tension is balanced closer to the migration front.

4.3. The cellular shear moment is also a dominant mechanical signal

M_s was of a similar order of magnitude as M_c (Fig. 1j,k).

Although both M_c and M_s have contributions from all traction components, the relationship between F_s^{RMS} and M_s was strongest (Fig. S5). In that the cells within the lowest quintile of F_s^{RMS} had negligible M_s and the cells within the highest quintile of F_s^{RMS} had a much larger M_s (Fig. S5e).

4.4. The mechanical state of highly circular cells includes signatures of a solid-like behavior

The mechanical state of the cells with higher circularity included lower $\tilde{F}_n$, F_s^{RMS}, M_c/Area, and M_s/Area (Fig. 2a,c,e,g). Interestingly, the cellular circularity was independent of R^{SD}, θ_{CM}, and v^{RMS}, and higher circularity was associated with weaker plithotaxis (Fig. S6). Coincidentally, cellular circularity increasing and approaching the value of 0.866 is a structural signature that the monolayer approaching a jamming transition, where individual cells are able to fluctuate but unable to change places with immediate neighbors [20]. Increased cellular density makes cellular motion structurally correlated over a wider area, an indicator of an approach to jamming transition [6]. Collectively, these properties are reminiscent of the particles of a jammed matter that withstands small shear stress [21]. Overall, the mechanical state of the cells with higher circularity indicates the need to use the approach described here combined with assessment of the cooperativity of cellular motion, and shear modulus of the cells to critically examine their solid-like behavior [6,22].

4.5. The mechanical state of fast-moving cells includes signatures of a fluid-like behavior

The mechanical state of the fast-moving cells included higher F_s^{RMS}, and M_s/Area (Fig. 2d,h). These properties are reminiscent of an external shear stress-driven motion of a viscous fluid. In addition, fast-moving cells are located closer to the migration front where cellular density is low (Fig. 1d,l). Collectively, these properties are reminiscent of the particles of a jammed matter gaining the ability to change places with immediate neighbors when exposed to high shear stress [6,21]. In addition, the association of faster motion with lower M_c/Area is reminiscent of the cells that generate lower contractile forces due to cytoskeletal fluidization (Fig. 2f) [23]. Overall, the mechanical state of fast-moving cells indicates the need to use the approach described here combined with visualization of subcellular motion and cellular contractile apparatus including cytoskeletal architecture to critically examine their fluid-like behavior [24,25].

4.6. The potential use of intercellular traction orientation to develop predictive models for monolayers

R^{SD} distinguished v^{RMS} and M_c more strongly than $\tilde{R}$ (Fig. 3a,b,d,e). By contrast, $\tilde{R}$ distinguished M_s more strongly than R^{SD} (Fig. 3c,f). As such, a mechanical or biochemical intervention that increases R^{SD} will tend to increase v^{RMS}, reduce M_c, and increase M_s. But an intervention that does not increase R^{SD} but instead increase $\tilde{R}$ will tend to have little effect on v^{RMS} and M_c, but it will tend to increase M_s. These findings and expectations can guide the development of theoretical models that can predict the mechanical state of the cell in response to mechanical and biochemical interventions or predict the behavior of a cell that is in a homogeneous versus heterogeneous microenvironment [11].

4.7. Cellular plithotaxis

The key observation of plithotaxis is that in a crowded environment of a monolayer, each constituent cell tends to migrate along the local axis of maximum principal stress. Plithotactic tendency is strongest at the locations where the anisotropy of the monolayer stress, or equivalently, the local maximum shear stress is highest [6]. However, along the axis of maximum principal stress, shear stress is necessarily zero. Hence, in plithotaxis, the collective significance of the role of zero shear stress along the preferred axis of motion and large maximum shear stress at the mechanically-steered locations remain unclear. One key question is whether the intercellular interfaces coincide with local axis of zero shear stress. The source of such knowledge gaps is that the picture of plithotaxis is identified using local subcellular analysis [6]. But access to cellular moments enabled us to reframe plithotaxis as a property of individual cells. In this process, we replaced the axis of maximum principal stress with the axis of M^{max}, and also replaced the orientation of local velocity vector with the orientation of v_i. This cellular plithotaxis is an *innately collective tendency of individual cells in a monolayer to migrate along the axis of maximum contractile moment*. Mapping F_s showed that the intercellular interfaces rarely coincided with the local axis of zero shear stress. On the contrary, larger $\tilde{R}$ was associated with stronger plithotaxis (Fig. 4c).

Cellular plithotaxis revealed additional useful insights. While cellular plithotaxis was associated with intercellular tractions, it was not associated with substrate tractions (Fig. 4a–d). Cells exhibiting stronger plithotaxis moved faster and had lower circularity (Figs.4g and S6d). However, the faster motion was not related to cellular alignment with either the axis of motion or the axis of the maximum principal moment (Fig. S7). Finally, plithotaxis was not associated with cells moving along their long axis, but cellular alignment along the maximum principal moment and cellular alignment with velocity went hand-in-hand (Figs. 4h and S4).

4.8. Unleashing shear

Cells in an advancing monolayer tended to generate high intrinsic "shear forces" (F_s and M_s). These shear forces were strongly associated with cellular plithotaxis and tended to increase cellular speed. In a way, individual cells within a monolayer are unleashed, i.e., *they move faster*, when neighbors unleash, i.e., *impose*, shear forces on them. In addition to such unleashing of and by shear forces, the data suggest the need to unleash the term "shear forces", i.e., *expand its scope*. In the field of endothelial biology, the term "shear forces" has long been used exclusively for the forces exerted by viscous fluid flowing over the cells. However, the current study suggests making that term inclusive of intercellular shear and apply it to guide our understanding of intercellular interactions.

The framework presented here can be used to examine how the relationships described here hold in other cellular systems or in quiescent monolayers, and how the three shear stresses — fluid shear stress, cell-substrate tractions, and intercellular shear traction — compete in disrupting or restoring endothelial homeostasis.

Declaration of competing interest

The authors declare no conflict of interest.

Appendix A. Supplementary data

Supplementary data to this article can be found online at https://doi.org/10.1016/j.bbrc.2019.11.048.

References

[1] R.B. Wysolmerski, D. Lagunoff, Involvement of myosin light-chain kinase in endothelial cell retraction, Proc. Natl. Acad. Sci. 87 (1990) 16–20.

[2] A. Krogh, Studies on the physiology of capillaries: II. The reactions to local stimuli of the blood-vessels in the skin and web of the frog, J. Physiol. 55 (1921) 412–422.

[3] D. Ragan, E. Schmidt, I. MacDonald, A. Groom, Spontaneous cyclic contractions of the capillary wall in vivo, impeding red cell flow: a quantitative analysis: evidence for endothelial contractility, Microvasc. Res. 36 (1988) 13–30.

[4] S.M. Dudek, J.G.N. Garcia, Cytoskeletal regulation of pulmonary vascular permeability, J. Appl. Physiol. 91 (2001) 15.

[5] X. Trepat, M.R. Wasserman, T.E. Angelini, E. Millet, D.A. Weitz, J.P. Butler, J.J. Fredberg, Physical forces during collective cell migration, Nat. Phys. 5 (2009) 426–430.

[6] D.T. Tambe, C.C. Hardin, T.E. Angelini, K. Rajendran, C.Y. Park, X. Serra-Picamal, E.H. Zhou, M.H. Zaman, J.P. Butler, D.A. Weitz, J.J. Fredberg, X. Trepat, Collective cell guidance by cooperative intercellular forces, Nat. Mater. 10 (2011) 469–475.

[7] D.T. Tambe, U. Croutelle, X. Trepat, C.Y. Park, J.H. Kim, E. Millet, J.P. Butler, J.J. Fredberg, Monolayer stress microscopy: limitations, artifacts, and accuracy of recovered intercellular stresses, PLoS One 8 (2013), e55172.

[8] C.C. Hardin, J. Chattoraj, G. Manomohan, J. Colombo, T. Nguyen, D. Tambe, J.J. Fredberg, K. Birukov, J.P. Butler, E. Del Gado, R. Krishnan, Long-range stress transmission guides endothelial gap formation, Biochem. Biophys. Res. Commun. 495 (2018) 749–754.

[9] R. Steward Jr., D.T. Tambe, C.C. Hardin, R. Krishnan, J.J. Fredberg, Fluid shear, intercellular stress, and endothelial cell alignment, Am. J. Physiol. Cell Physiol. 308 (2015) C657–C664.

[10] N.G. Patel, A.B. Ysasi, S.J. Mentzer, A. Tsuda, D.T. Tambe, Development of a toolkit to visualize the components of local junctional forces in lung cells, Invited presentation and paper, Computational Methods for Predictive Medicine, in: IEEE Int. Conf. Biomed. Health Inform., Orlando, Florida, USA, 2017, p. 1. https://embs.papercept.net/conferences/conferences/BHI17/program/BHI17_ContentListWeb_1.html#thb2_05.

[11] G. Patel, N. Xu, A. Nguyen, D.F. Alvarez, J.J. Fredberg, T. Stevens, D.T. Tambe, Mechanical signaling in a pulmonary microvascular endothelial cell monolayer, Biochem. Biophys. Res. Commun. 519 (2019) 337–343.

[12] R.J. Leiphart, D. Chen, A.P. Peredo, A.E. Loneker, P.A. Janmey, Mechanosensing at cellular interfaces, Langmuir 35 (2019) 7509–7519.

[13] Z.M. Goeckeler, R.B. Wysolmerski, Myosin light chain kinase-regulated endothelial cell contraction: the relationship between isometric tension, actin polymerization, and myosin phosphorylation, J. Cell Biol. 130 (1995) 613–627.

[14] Z. Liu, J.L. Tan, D.M. Cohen, M.T. Yang, N.J. Sniadecki, S.A. Ruiz, C.M. Nelson, C.S. Chen, Mechanical tugging force regulates the size of cell-cell junctions, Proc. Natl. Acad. Sci. U. S. A 107 (2010) 9944–9949.

[15] C.A. Reinhart-King, M. Dembo, D.A. Hammer, The dynamics and mechanics of endothelial cell spreading, Biophys. J. 89 (2005) 676–689.

[16] J.P. Butler, I.M. Tolic-Norrelykke, B. Fabry, J.J. Fredberg, Traction fields, moments, and strain energy that cells exert on their surroundings, Am. J. Physiol. Cell Physiol. 282 (2002) C595–C605.

[17] R. Krishnan, D.D. Klumpers, C.Y. Park, K. Rajendran, X. Trepat, J. van Bezu,

V.W. van Hinsbergh, C.V. Carman, J.D. Brain, J.J. Fredberg, J.P. Butler, G.P. van Nieuw Amerongen, Substrate stiffening promotes endothelial monolayer disruption through enhanced physical forces, Am. J. Physiol. Cell Physiol. 300 (2011) C146–C154.

[18] C. Grashoff, B.D. Hoffman, M.D. Brenner, R. Zhou, M. Parsons, M.T. Yang, M.A. McLean, S.G. Sligar, C.S. Chen, T. Ha, M.A. Schwartz, Measuring mechanical tension across vinculin reveals regulation of focal adhesion dynamics, Nature 466 (2010) 263–266.

[19] N.M. Morel, A.B. Dodge, W.F. Patton, I.M. Herman, H.B. Hechtman, D. Shepro, Pulmonary microvascular endothelial cell contractility on silicone rubber substrate, J. Cell. Physiol. 141 (1989) 653–659.

[20] D. Bi, X. Yang, M.C. Marchetti, M.L. Manning, Motility-driven glass and jamming transitions in biological tissues, Phys. Rev. X 6 (2016).

[21] A.J. Liu, S.R. Nagel, The jamming transition and the marginally jammed solid, Annu. Rev. Condens. Matter Phys. 1 (2010) 347–369.

[22] O. Kilic, A. Yoon, S.R. Shah, H.M. Yong, A. Ruiz-Valls, H. Chang, R.A. Panettieri, S.B. Liggett, A. Quiñones-Hinojosa, S.S. An, A. Levchenko, A microphysiological model of the bronchial airways reveals the interplay of mechanical and biochemical signals in bronchospasm, Nat. Biomed. Eng. 3 (2019) 532–544.

[23] R. Krishnan, E.P. Canović, A.L. Iordan, K. Rajendran, G. Manomohan, A.P. Pirentis, M.L. Smith, J.P. Butler, J.J. Fredberg, D. Stamenović, Fluidization, resolidification, and reorientation of the endothelial cell in response to slow tidal stretches, Am. J. Physiol. Cell Physiol. 303 (2012) C368–C375.

[24] M. Guo, A.J. Ehrlicher, M.H. Jensen, M. Renz, J.R. Moore, R.D. Goldman, J. Lippincott-Schwartz, F.C. Mackintosh, D.A. Weitz, Probing the stochastic, motor-driven properties of the cytoplasm using force spectrum microscopy, Cell 158 (2014) 822–832.

[25] J. Riedl, A.H. Crevenna, K. Kessenbrock, J.H. Yu, D. Neukirchen, M. Bista, F. Bradke, D. Jenne, T.A. Holak, Z. Werb, M. Sixt, R. Wedlich-Soldner, Lifeact: a versatile marker to visualize F-actin, Nat. Methods 5 (2008) 605–607.